# Crystal Growth and Optical and Spectroscopic Characterization of the Ytterbium-Doped Laser Molybdate Yb−$Li_3Gd_3Ba_2(MoO_4)_8$

Alberto García-Cortés and Concepción Cascales*

*Instituto de Ciencia de Materiales de Madrid CSIC, c/Sor Juana Inés de la Cruz, 3, Cantoblanco, 28049 Madrid, Spain*

*Received November 2, 2007. Revised Manuscript Received April 8, 2008*

Because of the existence of a phase transition at temperatures lower than the melting point, Yb-doped $Li_3Gd_3Ba_2(MoO_4)_8$ was grown by the top seeded solution growth slow cooling method using $Li_2Mo_2O_7$ as flux. At room temperature, the crystal possesses monoclinic symmetry with space group *C*2/*c* (No. 15), with lattice parameters $a = 5.2355(3)$ Å, $b = 12.7396(8)$ Å, $c = 19.1626(11)$ Å, and $\beta = 91.170(1)°$, and only one 8*f* crystal site for $Yb^{3+}$, which is shared with $Li^+$ and $Gd^{3+}$ cations. The information provided by the low temperature (6 K) spectroscopy indicates crystal field splittings of 0, 223, 353, and 460 $cm^{-1}$ and 10248, 10413, and 10634 $cm^{-1}$ for $^2F_{7/2}$ and $^2F_{5/2}$ $Yb^{3+}$ manifolds, respectively, and the spectral broadening observed is attributed to locally disordered environments around the 8*f* $Yb^{3+}$ centers. Ultraviolet and infrared optical absorption edges of this biaxial laser crystal also were characterized.

## Introduction

Diode-pumped solid state lasers based on $Yb^{3+}$-doped crystals are interesting alternatives to those based on $Nd^{3+}$ for CW tunable and ultrashort pulse[1,2] or high powered laser applications[3,4] in the wavelength range near 1 $\mu$m. Stronger interactions of $Yb^{3+}$ electronic states with lattice vibrations,[5] which lead to large homogeneous spectral broadening and to larger laser gain bandwidths, and smaller Stokes shifts with regards to $Nd^{3+}$ counterparts account for such functionalities and recognition of Yb-based lasers. The main disadvantage of $Yb^{3+}$ laser crystals is associated with the quite high threshold pump power required by the quasi-three-level room temperature operating laser scheme, but it can be overcome in crystal hosts producing adequately large ground state $^2F_{7/2}$ splitting through strong crystal field effects. Since the relation between spectroscopic characteristics and laser properties is particularly dependent on structural characteristics related to symmetry and bonding of the $Yb^{3+}$ site in the crystal framework, crystals with short bonding distances and/or largely distorted coordination polyhedra around $Yb^{3+}$ must be selected.[6]

On the other hand, wide tunable and ultrashort pulsed $Yb^{3+}$ laser emission can be expected in multisite hosts, that is, crystals with more than one crystallographic site occupied by $Yb^{3+}$, being favored specially by the existence of structural disorder around these sites, as has been previously demonstrated for $CaGdAlO_4$,[1] $SrY_4(SiO_4)_3O$,[7] and recently for tetragonal double tungstates (DT) and double molybdates (DM) $AT(XO_4)_2$ (A = monovalent Li or Na; T = trivalent Y, Gd, or Lu; and X = Mo or W),[2,8–10] derived from the total replacement of $Ca^{2+}$ in $CaXO_4$, all of them showing large inhomogeneous broadened spectral bands.

As an alternative to these DT and DM crystals, the partial substitution of the divalent cation D in the general $DXO_4$ formula leads to a number of compounds with more complex compositions, which can offer appropriate sites for $Yb^{3+}$ substitution, and additionally provide multiple distributions of cationic environments around these sites due to the coexistence of mono-, di-, and trivalent cations located in them. Inspecting already known compositions for ternary molybdates[11] with the indicated desirable structural characteristics, $Li_3Gd_3Ba_2(MoO_4)_8$ (hereafter, LiGdBaMo) results in being a suitable crystal phase. Its structural description[12] in the monoclinic space group *C*2/*c* (No. 15) indicated the existence of two crystal point sites for $Gd^{3+}$, with very different symmetries, 8*f* and 4*e*. Moreover, both sites are shared, the general 8*f* site being simultaneously occupied by $Li^+$, $Gd^{3+}$, and $Ba^{2+}$, and the special 4*e* site occupied by $Gd^{3+}$ and $Ba^{2+}$ cations. Around these crystal sites, the

* Corresponding author. E-mail: ccascales@icmm.csic.es.

(1) Zaouter, Y.; Didierjean, J.; Balembois, F.; Leclin, G. L.; Druon, F.; Georges, P.; Petit, J.; Goldner, P.; Viana, B. *Opt. Lett.* **2006**, *31*, 119.
(2) García-Cortés, A.; Cano-Torres, J. M.; Serrano, M. D.; Cascales, C.; Zaldo, C.; Rivier, S.; Mateos, X.; Griebner, U.; Petrov, V. *IEEE J. Quantum Electron.* **2007**, *43*, 758.
(3) Giesen, A.; Hügel, H.; Voss, A.; Wittig, K.; Brauch, U.; Opower, H. *Appl. Phys. B: Lasers Opt.* **1994**, *58*, 363.
(4) Liu, J.; Petrov, V.; Mateos, X.; Zhang, H.; Wang, J. *Opt. Lett.* **2007**, *32*, 2016.
(5) Ellens, A.; Andres, H.; Meijerink, A.; Blasse, G. *Phys. Rev. B: Condens. Matter Mater. Phys.* **1997**, *55*, 173. Ellens, A.; Andres, H.; ter Heerdt, M. L. H.; Wegh, R. T.; Meijerink, A.; Blasse, G. *Phys. Rev. B: Condens. Matter Mater. Phys.* **1997**, *55*, 180.
(6) Haumesser, P. H.; Gaumé, R.; Viana, B.; Antic-Fidancev, E.; Vivien, D. *J. Phys.: Condens. Matter* **2001**, *13*, 5427.
(7) Druon, F.; Balembois, F.; Georges, P. *Opt. Express* **2004**, *12*, 5005.
(8) Rico, M.; Griebner, U.; Petrov, V.; Ortega, P.; Xiumei, H.; Cascales, C.; Zaldo, C. *J. Opt. Soc. Am. B* **2006**, *23*, 1083.
(9) Cascales, C.; Serrano, M. D.; Esteban-Betegon, F.; Zaldo, C.; Peters, R.; Johannsen, J.; Mond, M.; Peterman, K.; Huber, G.; Ackermann, L.; Rytz, D.; Dupré, C.; Rico, M.; Griebner, U.; Petrov, V. *Phys. Rev. B: Condens. Matter Mater. Phys.* **2006**, *74*, 174114.
(10) García Cortés, A.; Han, X.; Cano-Torres, J. M.; Cascales, C.; Zaldo, C.; Mateos, X.; Petrov, V.; Valle, F. J. *J. Appl. Phys.* **2007**, *101*, 63110.
(11) Inorganic Crystal Structure Database ICSD, Fachinformationszentrum-Karlsruhe, Germany, 2006.
(12) Kletsova, R. F.; Vasil'ev, A. D.; Glinskaya, L. A.; Kruglik, A. I.; Kozhevnikova, N. M.; Korsun, V. P. *J. Struct. Chem.* **1992**, *33*, 443.

10.1021/cm703138x CCC: $40.75 
Published on Web 05/27/2008

corresponding Gd(Yb)1$O_8$ and Gd(Yb)2$O_{10}$ polyhedra present extended ranges of Gd(Yb)−O bonding distances, from 2.374 to 2.508 Å and from 2.684 to 3.079 Å, respectively. The distortion degree of the last polyhedron, estimated as $\Delta d = 1/10\Sigma(d_i - d_{av}/d_{av})^2$ [ref 13], is very high, $22.5 \times 10^{-3}$, and it could be indicative of a strong crystal field interaction for the 4*e* site, thus yielding large $^2F_{7/2}$ splitting, which along with the expected structural disorder could provide large spectral bandwidths. In fact, $Nd^{3+}$-doped LiGdBaMo has been reported as a structurally disordered laser crystal,[14] for which continuous and passive Q-switching diode-pumped laser operation has been demosnstrated.[15]

In this paper, we present results on the study of the thermal stability of the monoclinic *C*2/*c* phase of LiGdBaMo:Yb and, thus, the conditions for successful growth by the slow cooling top seeded solution growth (TSSG) method of adequate large crystals for spectroscopic and laser experiments. The crystallographic structure of the grown crystal was studied by single crystal X-ray diffraction. The transparency range of the crystal and the sequence of $Yb^{3+}$ energy levels determined from low temperature (6 K) polarized optical absorption and photoluminescence spectra, and further assessed with predictive structure-based simulations of crystal field interactions, are also reported.

## Experimental Techniques

**Preparation of Polycrystalline Samples and Crystal Growth.** Required stoichiometric amounts of analytical-grade $BaO_2$, $Li_2CO_3$, $MoO_3$, $Gd_2O_3$, and $Yb_2O_3$ were used in the synthesis of LiGdBaMo:Yb and $Li_2Mo_2O_7$, the polycrystalline precursor (solute) and the utilized flux, respectively. Lanthanide sesquioxides were 99.99% Alfa Aesar reagents. The preparation of the solute and flux as well as the TSSG slow cooling experiments were made using Pt crucibles and a vertical tubular furnace with $Si_2Mo$ as the heating element. The temperature was set with a resolution better than ±0.2 °C using an Eurotherm 818P temperature controller. To test the purity of the crystal phases, standard room temperature X-ray powder diffraction (XRPD) analysis of both synthesized polycrystalline solute and flux was performed with a Bruker AXS D-8 Advance diffractometer, using Cu Kα radiation. 2$\theta$ scans were made in the angular range of $5° \leq 2\theta \leq 80°$, with $\Delta 2\theta = 0.02°$ steps and a counting time of 2 s per step.

Thermal analyses were made by differential scanning calorimetry (DSC) in a Setaram SetSys Evolution 1700 DTG-DSC system. Amounts of ∼50 mg of mixtures of the solute with the flux in several selected ratios were heated and cooled in complete thermal cycles to determine the most adequate composition of the solute−flux mixture to perform the growth process. Furthermore, the thermal stability of the polycrystalline precursor was checked through two complete heating/cooling thermal cycles. Pt crucibles and a constant argon flow were used. The crystal habit and morphology of grown crystals were simulated with Donnay−Harker-based SHAPE software.[16]

**Single Crystal XRD Analysis.** A prismatic colorless suitable single crystal cut from the grown LiGdBaMo:Yb crystal was mounted on a Bruker SMART CCD diffractometer equipped with a normal focus 3 kW sealed tube. Data were collected at room temperature over a hemisphere of the reciprocal space by a combination of three sets of exposures. Each set had a different angle for the crystal, and each exposure of 20 s covered 0.3° in $\omega$. The crystal−detector distance was 5.01 cm. The unit cell parameters were determined by a least-squares fit of ∼40 reflections with $I > 20\sigma(I)$. Neutral-atom scattering factors for all atoms were used, and anomalous dispersion corrections were applied.[17] The structure was solved by direct methods. Special positions of Li atoms were located in difference Fourier maps. SADABS absorption correction was applied at the end of cycles of isotropic refinement. Refinement was for full-matrix least-squares analysis, with anisotropic thermal parameters for all atoms except Li, which was isotropically refined. The calculations were performed using the SHELXTL program,[18] and the views of the structure were drawn with the ATOMS software.[19]

**Spectroscopic Characterization.** For optical measurements, the crystals were oriented by Laue X-ray diffraction patterns, cut, and polished with diamond paste. Simulations of the Laue patterns were obtained with LAUE.[20] Optical absorption measurements were made in a Varian spectrophotometer model Cary 5E ($\lambda = 200-3000$ nm) and with a Bruker spectrophotometer (model IFS66v/S, $\lambda = 1.3-200\ \mu$m). The sample temperature was varied in the 6−300 K range by using a He closed-cycle Oxford cryostat equipped with the proper temperature controller. For polarized measurements, the sample was inserted between a Glan−Taylor polarizer and a depolarizer sheet. The spectra were measured with electric field components of the light parallel to each one of the three crystallographic axes, *E*//*a*, *E*//*b*, and *E*//*c*. The photoluminescence was excited with a Ti-sapphire laser, dispersed in a SPEX 340-E spectrometer ($f = 34$ cm), and detected with a 77 K cooled Ge photodiode and a lock-in amplifier.

## Results and Discussion

**Synthesis and Crystal Growth.** A nominal 10 mol % Yb-doping level in LiGdBaMo, comparable to its concentration in previous DT[2,9,10,21,22] and DM,[8,23,24] was chosen. To prepare a suitable polycrystalline precursor, isostructural with the phase previously described,[12] the obtained products of several thermal treatments, from 500 °C to the melting temperature, with annealing times of 48 h to 2 weeks were monitored by XRPD. A well-crystallized sample with the features of the PDF 77-0830 pattern[25] can be obtained from 550 to 650 °C, the lower temperatures requiring longer

(13) Shannon, R. D.; Gummerman, P. S.; Chenavas, J. *J. Am. Miner.* **1975**, *60*, 714.
(14) Kaminskii, A. A. *Crystalline Lasers: Physical Properties and Operating Schemes*; CRC Press: Boca Raton, FL, 1996.
(15) Batay, L. E.; Demidovich, A. A.; Kuzmin, A. N.; Ryabtsev, G. I.; Strêk, W.; Titov, A. N. *Spectrochim. Acta, Part A* **1998**, *54*, 2117.
(16) Dowty, E. *SHAPE for Windows, Software for Drawing Crystal Shapes, v.7.2.1*; 2006.
(17) *International Tables for Crystallography*; Kynoch Press: Birmingham, U.K., 1974; Vol. 4.
(18) *SHELXTL Version 6.10 Software Package*; Siemens Energy and Automation Inc. Analytical Instrumentation: Madison, WI, 1998.
(19) Dowty, E. *ATOMS v. 5.1, Computer Program for Displaying Atomic Structures*; Kingsport, TN, 2001.
(20) Marín, C.; Dieguéz, E. *LAUE Software, in Orientation of Single Crystals by Back-Reflection Laue Pattern*; World Scientific: Singapore, 1999.
(21) Rico, M.; Liu, J.; Griebner, U.; Petrov, V.; Serrano, M. D.; Estebán-Betegón, F.; Cascales, C.; Zaldo, C. *Opt. Express* **2004**, *12*, 5362.
(22) Liu, J.; Cano-Torres, J. M.; Estebán-Betegón, F.; Serrano, M. D.; Cascales, C.; Zaldo, C.; Rico, R.; Griebner, U.; Petrov, V. *Opt. Laser Technol.* **2007**, *39*, 558.
(23) Liu, J.; Cano-Torres, J. M.; Cascales, C.; Estebán-Betegón, F.; Serrano, M. D.; Volkov, V.; Zaldo, C.; Rico, R.; Griebner, U.; Petrov, V. *Phys. Status Solidi A* **2005**, *202* (4), 29.
(24) Rico, M.; Liu, J.; Cano-Torres, J. M.; García-Cortés, A.; Cascales, C.; Zaldo, C.; Griebner, U.; Petrov, V. *Appl. Phys. B: Lasers Opt.* **2005**, *81*, 621.
(25) JCPDS-ICDD card file 77-0830 for $Li_3Gd_3Ba_2(MoO_4)_8$.

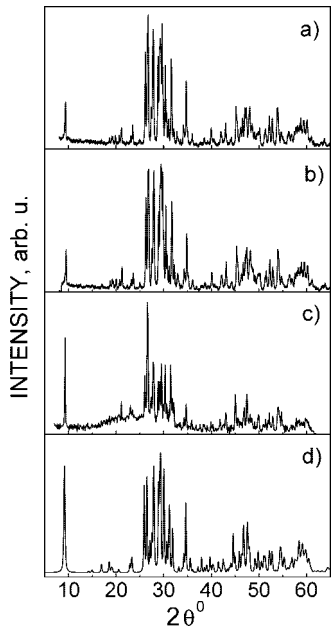


**Figure 1.** Room-temperature XRD patterns of (a) LiGdBaMo:Yb polycrystalline precursor synthesized at 600 °C for 2 days; (b) same sample with an additional annealing at 700 °C for 1 day; (c) grounded sample from LiGdBaMo:Yb melted at 960 °C; and (d) simulated pattern for $Gd_2Ba(MoO_4)_4$ (Cu Kα = 1.5406 Å).

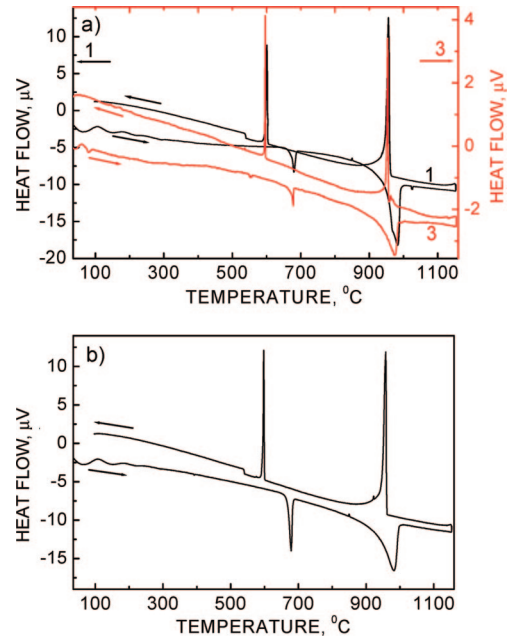


**Figure 2.** DSC curves of heating/cooling cycles of the LiGdBaMo:Yb polycrystalline precursor: (a) at a scanning rate of 10 °C $min^{-1}$ (1, black) and 3 °C $min^{-1}$ (3, red) and (b) second cycle at 10 °C $min^{-1}$.

annealing times. It was observed that XRPD patterns corresponding to samples synthesized at higher temperatures show only small changes (see Figure 1), involving slightly different distributions of the intensity *I* of *hkl* peaks, which could be attributed to the progressive loss of Li and would finally yield $Gd_2Ba(MoO_4)_4$:Yb (see the simulated XRPD pattern also included in Figure 1). $Gd_2Ba(MoO_4)_4$ has a $Nd_2Ba(MoO_4)_4$-type structure,[26] with monoclinic symmetry of space group *C*2/*c* and unit cell parameters $a = 5.263$ Å, $b = 19.33$ Å, $c = 12.677$ Å, and $\gamma = 91.399$ °.[27] The XRDP pattern of the melted at 960 °C product is similar to the previous ones, and the intensity differences observed in *hkl* peaks with regards to LiGdBaMo:Yb polycrystalline powders synthesized at low temperatures are more likely due to texturing than to the presence of $Gd_2Ba(MoO_4)_4$ achieved after a complete loss of Li. The clear distinction between both crystal phases—or the account of any additional overlapping new ones—is not straightforward given the high density of reflections and their match because of the closeness between both unit cell parameters. In any case, these results indicate that the LiGdBaMo:Yb crystal must be grown at adequately low temperatures to discard any eventual Li volatilization.

In tandem with the XRPD analyses, the thermal stability and possible phase transitions of LiGdBaMo:Yb were studied by DSC. Figure 2 shows the dependence of the polycrystalline LiGdBaMo:Yb precursor on heat flow with temperature (DSC curves) between 20 and 1150 °C. In the first heating/cooling cycle, at a scanning rate of 10 °C $min^{-1}$ (see Figure 2a-1), two endothermic peaks were observed during the heating, with maxima at 680 and 983 °C. The higher temperature peak corresponds to a solid−liquid transformation, also observed in crystal growth experiments. Upon cooling, the DSC curve shows two exothermic peaks, both sharper than in the heating run, with maxima at 956 and 601 °C, the first corresponding to the resolidification of LiGdBaMo:Yb. The temperature of these two exothermic peaks is shifted with regard to the corresponding endothermic peaks in the melting, especially considering the hysteresis for the observed lower temperature maxima, 79 °C (see Table 1).

The second cycle, Figure 2b, carried out with resulting material from the first cycle also at a scanning rate of 10 °C $min^{-1}$, presents a similar pattern, with endothermic peaks at 679 and 983 °C and exothermic maxima at 958 and 598 °C, the most noticeable changes being the rather broadened endothermic signal corresponding to the melt and the observed higher enthalpy change for the lower temperature phase transition in the heating path, now similar to the corresponding value upon cooling (see Table 1).

Along these two cycles, the temperatures of corresponding peaks are almost the same, and since no appreciable variation of weight was observed, it is possible to conclude that the existing crystal phases are the same in both cycles. Even if some slight loss of Li can be considered, yielding a Li-deficient LiGdBaMo:Yb composition, the presence of $Gd_2Ba(MoO_4)_4$:Yb as a decomposition product must be discarded since its melting point is expected to be 50−70 °C higher than for LiGdBaMo:Yb,[12] and it should be more apparent in the second heating cycle. Both stoichiometric ternary LiGdBaMo and double $Gd_2Ba(MoO_4)_4$ molybdate crystals have the same crystal structure, with *C*2/*c* symmetry, and their unit cell parameters are very close, but the latter has a distinctive congruent melting,[12] and in fact, $Gd_2Ba(MoO_4)_4$:Yb crystals for laser experiments recently were grown by the Czochralski method at 1070 °C.[28]

(26) Kiseleva, I. I.; Sirota, M. I.; Ozerov, R. I.; Balakireva, T. P.; Maier, A. A. *Kristallografiya* **1979**, *24*, 1277.
(27) JCPDS-ICDD card file 36-0192 for $Gd_2Ba(MoO_4)_4$.
(28) Haomiau, Z.; Yujin, C.; Yanfu, L.; Xinghong, G.; Qiguang, T.; Zundu, L.; Yindong, H. *J. Appl. Phys.* **2007**, *101*, 63109.

**Table 1. Characteristics of Thermal Behavior of the LiGdBaMo:Yb Polycrystalline Precursor**

| | | heating | | | cooling | | | |
|---|---|---|---|---|---|---|---|---|
| cycle | SR (°C $min^{-1}$)[a] | $T_{onset}$ (°C) | $T_{peak}$ (°C) | $\Delta H$ ($\mu$V s/mg) | $T_{onset}$ (°C) | $T_{peak}$ (°C) | $\Delta H$ ($\mu$V s/mg) | $\Delta T$ (°C) |
| 1[b] | 10 | 673.3 | 679.8 | 1.9151 | 603.8 | 601.1 | −4.9340 | 79 |
| | | 951.8 | 982.9 | 20.2646 | 960.9 | 956.1 | −17.9319 | 27 |
| 2[b] | 10 | 668.0 | 678.7 | 5.1875 | 599.8 | 597.8 | −5.1613 | 81 |
| | | 932.3 | 982.5 | 21.6909 | 961.3 | 957.9 | −19.8614 | 25 |
| 3[c] | 3 | 672.9 | 677.9 | 2.2221 | 597.4 | 596.1 | −5.2739 | 82 |
| | | 948.3 | 974.9 | 24.6390 | 955.9 | 954.1 | −16.0604 | 21 |

[a] SR: scanning rate. [b] Consecutively carried out experiments with the same LiGdBaMo:Yb polycrystalline power. [c] Experiment carried out with other amounts of LiGdBaMo:Yb polycrystalline powder.

The previously experimental findings suggest that a reversible first-order phase transformation at the temperature range of 600−680 °C exists for this ternary molybdate. Indeed, polymorphism is a well-known feature of triple and double molybdates and tungstates.[29,30] However, since no appreciable changes were detected in XRPD patterns taken for samples annealed for several hours (even days) at temperatures below and above this temperature range, the phase transition does not seem to correspond to a change in the crystal symmetry. Results of optical absorption measurements further confirm this point (see the Supporting Information). The isosymmetrical phase transition is possibly related to subtle geometrical changes in the framework, as those derived from tilting of the $MoO_4$ tetrahedra,[31] Jahn−Teller distortions in $LiO_6$ octahedra,[32] or their combined effects, among others, that could be associated with some charge ordering of $Li^+$ and $Gd^{3+}$ (ref 33) over the site that they simultaneously occupy.

To check if the hysteresis width of the two peaks depends on the scanning rate, a slower 3 °C $min^{-1}$ complete cycle was performed with another portion of the same polycrystalline precursor (see Figure 2a-3 for the DSC curve and Table 1 for the characteristics of the observed peaks). While the hysteresis for the first peak remains almost the same, some decrease in the melting-point hysteresis width, mainly due to the lessening of the temperature melting upon heating, can be detected. Subsequent heating/cooling cycles, or slow scanning rates, seem to diminish the temperature for melting.

The phase transition for LiGdBaMo:Yb prevents its crystal growth by the Czochralski technique. The TSSG slow cooling method and $Li_2Mo_2O_7$ as the flux, with the melting point adequately low, were used to grow these single crystals. Moreover, the use of this flux will compensate for any possible volatilization of Li and Li deficiency[34] in the grown crystal. The crystallization temperature, that is, the saturation temperature for different mixtures of LiGdBaMo:Yb and $Li_2Mo_2O_7$, was determined by DSC as the resolidification temperature after melting upon cooling, in each case. The results, the solubility curve for the used flux, can be observed in Figure 3. A mixture with a molar solute/flux ratio of 2.66:97.34, corresponding to 15 wt % solute and 85 wt % flux,

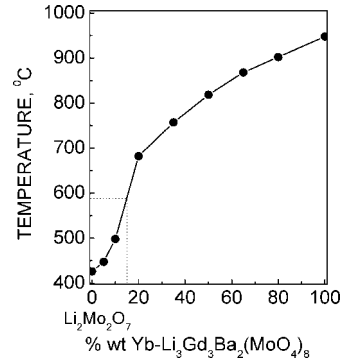


**Figure 3.** Solubility curve of LiGdBaMo:Yb in the $Li_2Mo_2O_7$ flux.

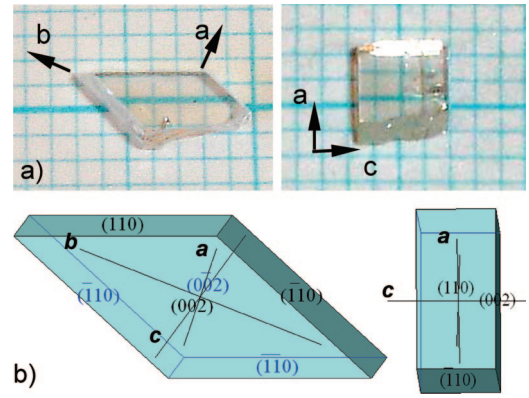


**Figure 4.** (a) LiGdBaMo:Yb TSSG grown crystal: (left) (001) oriented plate showing the spontaneously grown face and (right) (010)-cut sample. (b) Simulated morphology schemes of the crystal.

resulted in being the most suitable composition for crystal growth of LiGdBaMo:Yb crystals. This mixture allows the best control of the crystallization process (see Figure 3), and its melting occurs at a temperature that prevents any undesired phase transformation. For homogenization, the temperature was kept for 20 h at ≈50 °C above the melting temperature, and then it was decreased to the crystallization point. The cooling interval was 11 °C, and the cooling rate was 0.08 °C/h. A Pt wire was used as seed, and its rotation speed was 12 rpm. Transparent colorless crystals, with a rhombic prismatic shape (as shown in Figure 4a) were obtained. Other attempts to grow crystals from mixtures with a larger concentration of the solute, and thus higher temperature of melting, were unsuccessful due to the cracking of the crystal upon cooling, when the temperature of the phase transition was reached.

Figure 4b shows morphological schemes of the grown crystal indicating its faces and crystal axes, simulated

(29) Tomaszewski, P. E. *Phase Transitions* **1992**, *38*, 127.
(30) Colón, C.; Alonso Medina, A.; Fernández, F.; Sáez Puche, R.; Volkov, V.; Cascales, C.; Zaldo, C. *Chem. Mater.* **2005**, *17*, 6635.
(31) Allan, D. R.; Nelmes, R. J. *J. Phys.: Condens. Matter* **1992**, *4*, 395.
(32) Radaelli, P. G.; Cox, D. E.; Marezio, M.; Cheong, S.-W. *Phys. Rev. B: Condens. Matter Mater. Phys.* **1997**, *55*, 3015.
(33) Friese, K.; Kanke, Y.; Fitch, A. N.; Grzechnik, A. *Chem. Mater.* **2007**, *19*, 4882.
(34) McCaroll, W. H.; Greenblatt, M. *J. Solid State Chem.* **1984**, *54*, 282.

**Table 2. Crystal and Structure Refinement Data for $Li_{2.86}Gd_{2.90}Yb_{0.24}Ba_2(MoO_4)_8$**

| | |
|---|---|
| formula wt | 2062.93 |
| temp (K) | 296(2) |
| wavelength (Å) | 0.71073 |
| cryst syst | monoclinic |
| space group | *C*2/*c* (No. 15) |
| unit cell dimensions (Å) | $a = 5.2355(3)$ |
| | $b = 12.7396(8)$ |
| | $c = 19.1626(11)$ |
| | $\beta = 91.170(1)$ |
| vol (Å$^3$) | 1277.84(13) |
| *Z* | 2 |
| calcd density (g/cm$^3$) | 5.319 |
| absorption coefficient (mm$^{-1}$) | 14.594 |
| absorption correction | SADABS |
| *F*(000) | 1810 |
| cryst size (mm$^3$) | 0.20 × 0.15 × 0.10 |
| $\theta$ range for data collection (deg) | 3.20−29.23 |
| limiting indices | $-7 \le h \le 7$; $-17 \le k \le 17$; $-26 \le l \le 25$ |
| reflns collected | 5653 |
| independent reflns | 1582 ($R_{int} = 0.0332$) |
| refinement method | full-matrix least-squares on $F^2$ |
| data/restraints/params | 1582/1/111 |
| goodness-of-fit on $F^2$ | 1.210 |
| final *R* indices [$I > 2\sigma(I)$] | $R_1 = 0.0446$, $wR_2 = 0.1069$ |
| *R* indices (all data) | $R_1 = 0.0524$, $wR_2 = 0.1127$ |

according the Donnay−Harker law[35] with SHAPE software.[16] Required cell parameters and space groups were derived from the current single crystal X-ray refinement, as discussed in Crystalline Structure.

**Crystalline Structure.** The single crystal X-ray determination of the structure of the LiGdBaMo:Yb grown crystal was performed in the monoclinic space group *C*2/*c* (No. 15), and the atomic coordinates considered initially were those reported previously.[12] Features of coordination polyhedra for cations in this description of the structure previously were indicated.

On the basis of the starting formula, our initial structure determination located Ba and Li, each one fully occupying a different 4*e* site, Gd(Yb) and Li with occupancy factors (OF) fixed to 0.75:0.25 in one 8*f* site, and Mo1, Mo2, and the eight types of O in different 8*f* sites. The refinement yielded $R_1 = 0.0723$, with anisotropic displacement parameters for all atoms except Li in 4*e*, which was isotropically refined. In the next step, we further refined the OF over 8*f* sites for Gd, Yb, and Li cations, with the total population assumed to be 1. An improved $R_1$ value of 0.044 was obtained with OF (Gd/Yb/Li) = 0.725(4):0.060(3):0.215(5), also with anisotropic thermal parameters for all atoms except Li in 4*e*. Details of this refinement are included in Table 2. Final crystallographic data, atomic coordinates, and refined occupancy factors for Gd, Yb, and Li simultaneously occupying the 8*f* crystal site appear in Table 3, and selected bonds are given in Table 4. A table with anisotropic displacement parameters for all cations except Li(2) is available in the Supporting Information. From these results, the formula of the grown crystal should be written as $Li_{2.86}Gd_{2.90}Yb_{0.24}Ba_2(MoO_4)_8$.

Positions of peaks and their relative intensities in the XRPD profile generated using refined single crystal X-ray data agree with those of the prepared polycrystalline precursor (see Figure 5), which confirms the experimental procedure.

Thus, the cationic distribution achieved in the current refinement of the structure of LiGdBaMo:Yb corrects the previous one for this ternary molybdate host.[12] Our present results lead to the conclusion that $Gd^{3+}$ occupies only one crystallographic site, 8*f*, and when $Yb^{3+}$ replaces $Gd^{3+}$, a disordered local environment around the first one exists as derived from the coexistence of $Gd^{3+}$ and $Li^+$ cations over this site.

The crystalline structure is constituted by Gd(Yb)/$LiO_8$ distorted square antiprisms with $C_1$ symmetry, distorted $LiO_6$ octahedra and $BaO_{10}$ polyhedra (the latter two lying along the two-fold *b* crystal axis), and two kinds of distorted $MoO_4$

**Table 3. Atomic Coordinates (×10$^4$) and Equivalent Isotropic Displacement Parameters (Å$^2$ × 10$^3$) for the LiGdBaMo:Yb Crystal**

| | | *x* | *Y* | *Z* | OF | *U*(eq)[a] |
|---|---|---|---|---|---|---|
| Li(1) | 8*f* | 10020(1) | 1472(1) | 4680(1) | 0.215(5) | 13(1) |
| Gd(1) | 8*f* | 10020(1) | 1472(1) | 4680(1) | 0.725(4) | 13(1) |
| Yb(1) | 8*f* | 10020(1) | 1472(1) | 4680(1) | 0.060(3) | 13(1) |
| Ba | 4*e* | 10000 | 292(1) | 2500 | | 18(1) |
| Li(2) | 4*e* | 5000 | −1821(19) | 2500 | | 20(5) |
| Mo(1) | 8*f* | 9913(2) | 4403(1) | 4074(1) | | 13(1) |
| Mo(2) | 8*f* | 5011(2) | 2387(1) | 3494(1) | | 13(1) |
| O(1) | 8*f* | 12534(13) | 4821(6) | 4631(4) | | 18(1) |
| O(2) | 8*f* | 7657(12) | 5416(5) | 3949(4) | | 16(1) |
| O(3) | 8*f* | 7525(13) | 1459(5) | 3628(4) | | 18(1) |
| O(4) | 8*f* | 2717(14) | 1994(5) | 2870(4) | | 21(1) |
| O(5) | 8*f* | 3394(13) | 2604(6) | 4307(4) | | 19(1) |
| O(6) | 8*f* | 11259(13) | 4137(6) | 3272(4) | | 19(1) |
| O(7) | 8*f* | 6399(14) | 3552(5) | 3201(4) | | 20(1) |
| O(8) | 8*f* | 8468(14) | 3314(6) | 4522(4) | | 20(1) |

[a] *U*(eq) is defined as one third of the trace of the orthogonalized $U_{ij}$ tensor.

**Table 4. Selected Bond Lengths (Å) for LiGdBaMo:Yb[a]**

| | | | |
|---|---|---|---|
| T(1)/Li(1)−O(1)#1[b] | 2.474(7) | Mo(1)−O(1) | 1.802(7) |
| T(1)/Li(1)−O(1)#8 | 2.454(7) | Mo(1)−O(2) | 1.763(7) |
| T(1)/Li(1)−O(2) | 2.400(7) | Mo(1)−O(6) | 1.739(7) |
| T(1)/Li(1)−O(3) | 2.379(7) | Mo(1)−O(8) | 1.806(7) |
| T(1)/Li(1)−O(5)#6 | 2.401(7) | | |
| T(1)/Li(1)−O(5)#7 | 2.404(7) | Mo(2)−O(3) | 1.784(7) |
| T(1)/Li(1)−O(8) | 2.500(7) | Mo(2)−O(4) | 1.751(7) |
| T(1)/Li(1)−O(8)#7 | 2.421(7) | Mo(2)−O(5) | 1.809(7) |
| | | Mo(2)−O(7) | 1.750(7) |
| Li(2)−O(4)#3 | 2.183(19) | | |
| Li(2)−O(4)#4 | 2.183(19) | T(1)/Li(1)−T(1)/Li(1)#7 | 3.9320(11) |
| Li(2)−O(6)#1 | 2.017(17) | T(1)/Li(1)−T(1)/Li(1)#8 | 3.8707(11) |
| Li(2)−O(6)#2 | 2.017(17) | | |
| Li(2)−O(7)#1 | 2.358(9) | Ba−Li(2) | 3.755(18) |
| Li(2)−O(7)#2 | 2.358(9) | Ba#1−Li(2) | 3.68(2) |
| Ba−O(2)#2 | 3.083(7) | Ba−T(1)/Li(1) | 4.4395(11) |
| Ba−O(2)#4 | 3.083(7) | | |
| Ba−O(3) | 2.946(7) | T(1)/Li(1)#7−Mo(1) | 3.7230(9) |
| Ba−O(3)#11 | 2.946(7) | T(1)/Li(1)#8−Mo(1) | 3.7042(10) |
| Ba−O(4)#6 | 2.681(7) | T(1)/Li(1)#5−Mo(2) | 3.6870(9) |
| Ba−O(4)#9 | 2.681(7) | T(1)/Li(1)#7−Mo(2) | 3.7892(10) |
| Ba−O(6)#1 | 2.882(7) | | |
| Ba−O(6)#10 | 2.882(7) | Li(2)−Mo(1) | 3.365(7) |
| Ba−O(7)#2 | 2.685(7) | Li(2)−Mo(1) | 3.397(7) |
| Ba−O(7)#4 | 2.685(7) | Li(2)−Mo(2) | 3.416(7) |
| | | Li(2)−Mo(2) | 3.366(7) |

[a] Symmetry transformations used to generate equivalent atoms: #1: $x-1/2,y-1/2,z$. #2: $-x+3/2,y-1/2,-z+1/2$ #3: $-x+1/2,y-1/2,-z+1/2$. #4: $x+1/2,y-1/2,z$. #5: $x-1,y,z$. #6: $x+1,y,z$. #7: $-x+3/2,-y+1/2,-z+1$. #8: $-x+5/2,-y+1/2,-z+1$. #9: $-x+1,y,-z+1/2$. #10: $-x+5/2,y-1/2,-z+1/2$. #11: $-x+2,y,-z+1/2$. #12: $x+1/2,y+1/2,z$. #13: $x-1/2,y+1/2,z$. [b] T indicates Gd and Yb.

(35) Dowty, E. *Am. Mineral.* **1980**, *65*, 465.

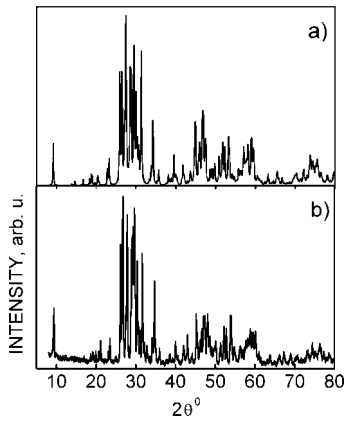


**Figure 5.** XRPD diagrams for (a) precursor calculated from single crystal X-ray data and (b) polycrystalline precursor LiGdBaMo:Yb.

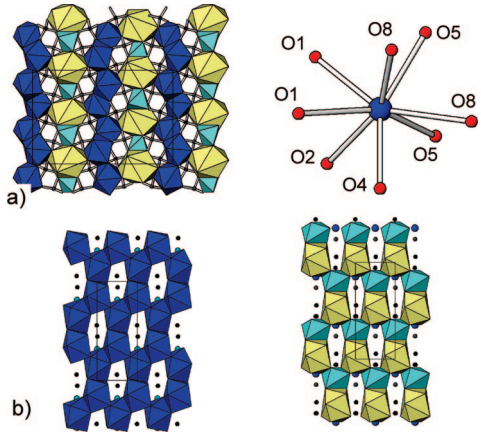


**Figure 6.** Structure of LiGdBaMo:Yb crystal: (a) left, *bc* plane view showing Gd(Yb)/$LiO_8$ distorted square antiprisms (blue), $LiO_6$ distorted octahedra (cyan), and $BaO_{10}$ polyhedra (yellow) and right, the $C_1$ Gd(Yb)/$LiO_8$ coordination polyhedron and (b) left, *ab* plane of six-membered rings of Gd(Yb)/$LiO_8$ and right, adjacent *ab* plane of six-membered rings $LiO_6$ and $BaO_{10}$.

tetrahedra (see Figure 6a). This can be envisaged in terms of layers perpendicular to the *c* axis formed by corrugated six-membered rings of Gd(Yb)/$LiO_8$ polyhedra, which share edges (Figure 6b, left). Adjacent layers are connected through $BaO_{10}$ polyhedra and $LiO_6$ octahedra, which form infinite planar layers, also constituted by shared-edge six-membered rings, with a $BaO_{10}$-$LiO_6$ $BaO_{10}$-$LiO_6$ sequence (Figure 6b, right). The $MoO_4$ tetrahedra are linked to both sides of each layer through common vertices. This distinctive layered arrangement along the *c* axis thus determines the observed shape of TSSG grown LiGdBaMo:Yb crystals.

This structure can be considered to be derived from Li insertion in vacant 4*e* positions in isostructural $Gd_2Ba(MoO_4)_4$,[26] as can be seen in Figure 7. These empty sites, aligned along the *b* axis between $BaO_{10}$ polyhedra, are composed of cavities limited by six oxygen vertices that provide an octahedral environment around Li cations. Similar Li insertion can be viewed in isostructural *C*2/*c* $LiRbBi_2(MoO_4)_4$[36] and in Li-doped triclinic α-$KDy(MoO_4)_2$.[37]

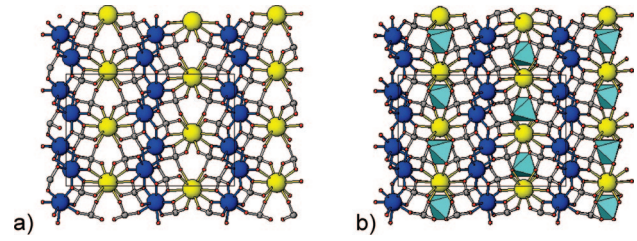


**Figure 7.** (a) View of the *bc* plane of monoclinic *C*2/*c* $Gd_2Ba(MoO_4)_4$. (b) View of the *bc* plane of isostructural LiGdBaMo:Yb showing the insertion of $LiO_6$ in octahedral cavities between $BaO_{10}$ polyhedra along the *b* axis.

Taking into consideration the characteristics of the structure of the LiGdBaMo:Yb crystal (i.e., $\beta \approx 90°$) and its layered nature perpendicular to the *c* direction, as well as the SHAPE[16] simulations of the growth habit, we established that the largest face of the TSSG grown crystals is perpendicular to the *c* axis. The comparison of experimentally obtained Laue patterns with those simulated[20] from the unit cell dimensions and symmetry of the crystal allowed us to identify the direction of the orthogonal *a* and *b* axes in the grown crystal, in the way that is indicated in Figure 4a.

In this monoclinic and thus biaxial crystal, one of the principal optical axes is parallel to the unique two-fold axis of the crystal, and the other two lie in a perpendicular plane to this axis. But, since the preparation of adequate prisms for precise measurements of refractive indices is problematic due to the cleavable nature of the crystal, for a description of the polarization characteristics, we can consider that its almost orthorhombic nature would suppose that there are two other optic axes practically aligned with the two remaining crystallographic axes. Hence, just for convenience of description, the three optical axes will be arbitrarily named by collinearity with the determined crystallographic axes. Spectra measurements thus were performed in configurations *E*//*a*, *E*//*b*, and *E*//*c*. After polishing, the as-grown crystal was used to measure the *E*//*a* and *E*//*b* spectra, while for *E*//*c* measurements, a polished *b* cut sample (see Figure 4a-right), from another TSSG crystal with the same characteristics, was used.

**Spectroscopic Characterization.** Figure 8 shows the transparency range of the LiGdBaMo:Yb crystal at room temperature and at 6 K. The absorption edge was determined from optical absorption (OA) measurements in the ultraviolet range, through linear extrapolation to zero of the stepping absorption in each case. Whereas at 300 K *E*//*a* and *E*//*c* OA spectra show less than a 1 nm difference, 348.0 and 347.6 nm, respectively, and narrow UV transparency for the *E*//*b* spectrum, 351.3 nm, at 6 K, the three polarizations present different and extended transparencies, 335.0, 337.0, and 333.1 nm for *E*//*a*, *E*//*b*, and *E*//*c*, respectively. The IR window extends up to the onset of multiphonon absorption, near 3.7 $\mu$m, related to $MoO_4$ vibrations.[38] It is worth noting that LiGdBaMo has a similar or larger bandgap than

(36) Kletsova, R. F.; Glinskaya, L. A.; Alekseev, V. I.; Khalbaeva, K. M.; Khaikina, E. G. *J. Struct. Chem.* **1993**, *34*, 789.
(37) Basovich, O. M.; Khaikina, E. G.; Solodovnikov, S. F.; Tsyrenova, G. D. *J. Solid State Chem.* **2005**, *178*, 580.
(38) Hanuza, J.; Maczka, M.; Hermanowicz, K.; Dereñ, P. J.; Strêk, W.; Folcik, L.; Drulis, H. *J. Solid State Chem.* **1999**, *148*, 468.

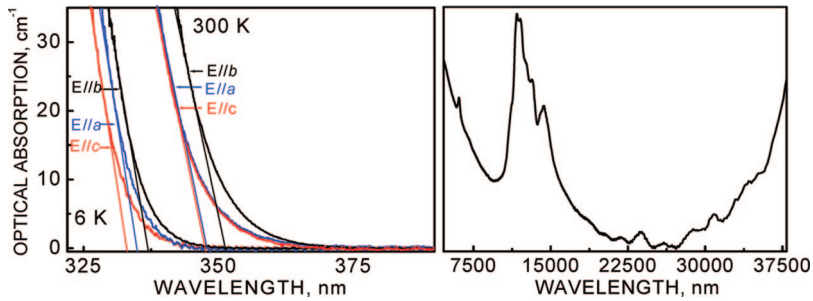


**Figure 8.** OA at 6 and 300 K of the LiGdBaMo:Yb single crystal. The straight lines in the polarized spectra at the UV limit were used to determine the effective bandgaps. For the 300 K unpolarized IR spectrum, the absorption scale is arbitrary.

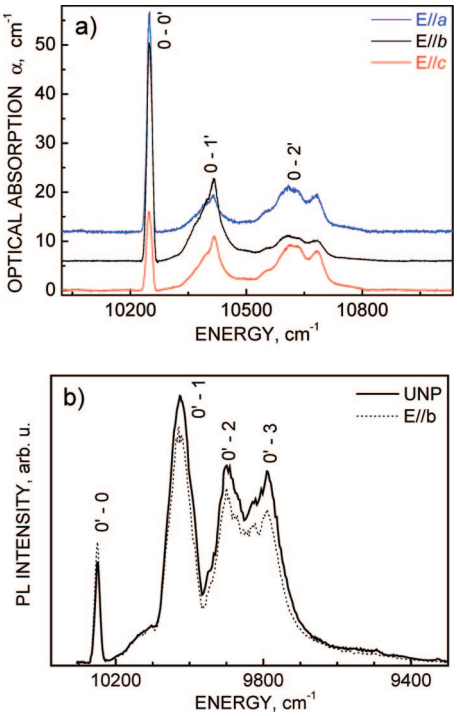


**Figure 9.** (a) 6 K absorption coefficient of LiGdBaMo:Yb crystal in the three polarizations (for the sake of clarity, the *y*-axis was displaced) and (b) 6 K PL excited at $\lambda_{exc} = 960$ nm, unpolarized and along the main polarization direction.

previously studied tetragonal double molybdate femtosecond laser crystal hosts.[8,39,40]

For the description of energy levels of the $4f^{13}$ configuration of $Yb^{3+}$ in LiGdBaMo, the low temperature (6 K) OA and photoluminescence (PL) spectra were measured. The $C_1$ local symmetry of the single 8*f* site of $Yb^{3+}$ in LiGdBaMo is expected to split the two multiplets $^2F_{7/2}$ ($n$) and $^2F_{5/2}$ ($n'$) into four ($n = 0, 1, 2, 3$) and three ($n' = 0', 1', 2'$) doubly degenerate Stark levels, respectively, all of them with irreducible representation $\Gamma_1$. For this point symmetry, no selection rules for *E*//*a*, *E*//*b*, and *E*//*c* polarizations exist, that is, all electric dipole (ED) or magnetic dipole (MD) transitions are allowed. Figure 9 shows the polarized 6 K OA spectra corresponding to $^2F_{7/2}$ (0) $\rightarrow$ $^2F_{5/2}$ ($n'$) transitions ($0 \rightarrow n'$) and the PL spectra for $^2F_{5/2}(0') \rightarrow {}^2F_{7/2}$ ($n$) ($0' \rightarrow n$) transitions. Although the observed peaks are the same in the three polarizations, the anisotropy for such biaxial crystals is important, with a clearly large OA for *E*//*a* and *E*//*b* spectra. The presence of a unique zero line absorption, $0 \leftrightarrow 0'$, agrees with the existence of a single 8*f* site for $Yb^{3+}$ ions in the LiGdBaMo crystal structure. However, even if this line is the sharpest one in the OA spectra, its observed FWHM is $\sim$19 $cm^{-1}$. For comparison, the fwhm of the same transition in ordered monoclinic Yb-$KY(WO_4)_2$ is $\sim$10 $cm^{-1}$.[41] This broadening is attributed to the structural short-range cationic disorder derived from $Yb^{3+}$ substitution over the shared crystal site, which creates a distribution of slightly different crystal fields around the $Yb^{3+}$ centers.

Despite its simplicity, the proclivity of the $4f^{13}$ electronic structure of $Yb^{3+}$ to interact with lattice vibrations[5] makes the identification of some of its energy levels difficult. While transitions observed in 6 K OA spectra at 10248 and 10413 $cm^{-1}$ can be straightforwardly assigned to $0 \rightarrow 0'$ and $0 \rightarrow 1'$ transitions, it is difficult to ascertain the energy of the $0 \rightarrow 2'$ transition in the complex 10550−10700 $cm^{-1}$ observed region, which must correspond to its mixture with vibronic sidebands. The observed bands in 6 K PL spectra, which correspond to $0' \rightarrow n$ transitions, also show some structure. Thus, for the confident identification of $Yb^{3+}$ energy levels, the interpretation of the 6 K spectra needs an assessment through predictive methods of crystal field (CF) interactions. The widely tested semiempirical CF simple overlap model (SOM),[42] which considers the structural characteristics of the first coordination shell around $Yb^{3+}$,[9,43] was used here to derive a proper set of CF parameters accounting for the CF potential of $Yb^{3+}$ in the LiGdBaMo crystal. Crystallographic data are from the previous X-ray analysis, and the effective charge for oxygen and magnitude of the overlap integral $\rho$ between $Yb^{3+}$ and oxygen wave functions were taken as −1.2 and 0.08, respectively.[42] Using SOM predicted CF parameters, the simulation of the sequence of energy levels was performed with a previously developed code.[44,45] It requires only two free-ion (FI) parameters, $E_0$ and the spin−orbit coupling constant $\zeta$, whose variation with the crystal host is theoretically weak, and

(39) Volkov, V.; Cascales, C.; Kling, A.; Zaldo, C. *Chem. Mater.* **2005**, *17*, 291.
(40) Rico, M.; Méndez-Blas, A.; Volkov, V.; Monge, M. A.; Cascales, C.; Kling, A.; Fernández-Díaz, M. T.; Zaldo, C. *J. Opt. Soc. Am. B* **2006**, *23*, 2066.
(41) Kuleshov, N. V.; Lagatsky, A. A.; Podlipensky, A. V.; Mikhailov, V. P.; Huber, G. *Opt. Lett.* **1997**, *22*, 1317.
(42) Porcher, P.; Couto dos Santos, M.; Malta, O. *Phys. Chem. Chem. Phys.* **1999**, *1*, 397.
(43) Cascales, C.; Sáez-Puche, R.; Zaldo, C. *Chem. Phys.* **1999**, *240*, 291.
(44) Cascales, C.; Antic-Fidancev, E.; Lemaitre-Blaise, M.; Porcher, P. *J. Phys.: Condens. Matter* **1992**, *4*, 2721.
(45) Cascales, C.; Sáez Puche, R.; Porcher, P. *J. Solid State Chem.* **1995**, *114*, 52.

**Table 5. Free Ion ($E^0$ and $\zeta$) and SOM Crystal Field ($B_q^k$, $S_q^k$) Parameters ($cm^{-1}$)[a] Used To Calculate Energy Levels (Italics) for the $Yb^{3+}$ (8*f* Site) in the LiGdBaMo Crystal[b]**

| | |
|---|---|
| $E^0$, $\zeta$ | 4628.04, 2901.60 |
| $B_0^2$, $B_2^2$ | 168, 88 |
| $B_0^4$, $B_2^4$, $S_2^4$, $B_4^4$, $S_4^4$ | −234, −401, −25, −589, −725 |
| $B_0^6$, $B_2^6$, $S_2^6$, $B_4^6$, $S_4^6$, $B_6^6$, $S_6^6$ | −34, −199, −241, −22, −150, −140, −201 |
| $^2F_{5/2}(2')$ | *10628*−10634 |
| $^2F_{5/2}(1')$ | *10422*−10413 |
| $^2F_{5/2}(0')$ | *10250*−10248 |
| $^2F_{7/2}(3)$ | *462*−460 |
| $^2F_{7/2}(2)$ | *392*−353 |
| $^2F_{7/2}(1)$ | *243*−223 |
| $^2F_{7/2}(0)$ | *0*−0 |

[a] Value for overlap integral $\rho$ between $Yb^{3+}$ and oxygen orbital wave functions is taken as 0.08, and the effective charge for oxygens is −1.2.[42] [b] Experimental energy levels appear at the right side of the column.

consequently can be reasonably adapted from previous values in the literature.[9] FI and SOM CF parameters and the resulting simulated sequence of $Yb^{3+}$ energy levels are summarized in Table 5. The agreement between the SOM calculated total splitting for $^2F_{7/2}$ (462 $cm^{-1}$) and the experimental energy difference between the first and the last peaks observed in the PL spectra (460 $cm^{-1}$), as well as for the energy positions of the bands of $0 \rightarrow 0'$ and $0 \rightarrow 1'$ transitions, confirms the reliability of the method and allows us to ascribe the peak observed in OA spectra at 10634 $cm^{-1}$ to the $0 \rightarrow 2'$ transition. The peak at 10687 $cm^{-1}$ in the same OA spectra would likely correspond to the coupling with a phonon of energy of ∼53 $cm^{-1}$. Thus, it is reasonable to consider phenomenological splitting schemes of 0, 223, 353, and 460 $cm^{-1}$ for the $^2F_{7/2}$ ground multiplet and 10248, 10413, and 10634 $cm^{-1}$ for the $^2F_{5/2}$ excited multiplet of $Yb^{3+}$ in LiGdBaMo. Moreover, their barycenters at 259 and 10432 $cm^{-1}$ are consistent with the relationship describing the barycentre law developed for $Yb^{3+}$.[6]

## Conclusion

The monoclinic (space group *C*2/*c*) LiGdBaMo:Yb crystal successfully was grown with optical quality by the TSSG method. The crystal structure has a single 8*f* site occupied simultaneously by $Gd^{3+}$ (72.5%), $Yb^{3+}$ (6%), and $Li^+$ (21.5%). This leads to a locally disordered environment around $Yb^{3+}$ ions, which generates the observed inhomogeneous broadening of the spectral features. From experimental spectroscopic results, it is clear that the CF splitting for the $^2F_{7/2}$ $Yb^{3+}$ ground multiplet is not so large as was thought initially. This is explained by the absence of the second 4*e* site for $Gd^{3+}$ ($Yb^{3+}$) cations in the crystal structure of LiGdBaMo, which would have produced the strongest CF effect on $Yb^{3+}$ energy levels. However, this splitting remains similar to that observed for $Yb^{3+}$ in tetragonal $NaT(WO_4)_2$ (T = Y,[2] Gd,[9] or Lu)[10] and in Yb-$LiGd(MoO_4)_2$,[8] all of them tunable lasers. Furthermore, the higher anisotropy of OA and PL polarized spectra would be responsible for absorption and emission cross-sections for specific crystal orientations of LiGdBaMo:Yb higher than in the previously mentioned tetragonal laser crystals.[46] On the other hand, the combination of disordered cationic environments around $Yb^{3+}$, with its electron−phonon coupling, can explain the observed tunability of 33 nm at the threshold of the laser oscillation in the LiGdBaMo:Yb crystal.[46]

**Acknowledgment.** This work was supported by Projects MAT2005-6354-C03-01 and MAT2008-06720-C02-01, Spain. A.G.-C. additionally acknowledges his FPU2003-3018 Spanish grant.

**Supporting Information Available:** LiGdBaMo:Yb crystal (CIF), additional table with anisotropic displacement parameters, and room-temperature optical absorption spectra of two samples of LiGdBaMo:Yb synthesized at 560 and 850 °C (PDF). This material is available free of charge via the Internet at http://pubs.acs.org.

CM703138X

(46) García-Cortés, A.; Zaldo, C.; Cascales, C.; Mateos, X.; Petrov, V. *Opt. Express* **2007**, *15*, 18162.